frontiers in Physics

ORIGINAL RESEARCH
published: 09 November 2020
doi: 10.3389/fphy.2020.578662

Single Molecule Localization Microscopy Analyses of DNA-Repair Foci and Clusters Detected Along Particle Damage Tracks

Michael Hausmann[1], Charlotte Neitzel[1], Elizaveta Bobkova[1], David Nagel[1], Andreas Hofmann[2], Tatyana Chramko[3], Elena Smirnova[3], Olga Kopečná[4], Eva Pagáčová[4], Alla Boreyko[3], Evgeny Krasavin[3], Iva Falkova[4], Dieter W. Heermann[2], Götz Pilarczyk[1], Georg Hildenbrand[1], Felix Bestvater[5] and Martin Falk[4]**

[1]Kirchhoff-Institute for Physics, Heidelberg University, Heidelberg, Germany, [2]Institute for Theoretical Physics, Heidelberg University, Heidelberg, Germany, [3]Joint Institute for Nuclear Research, Dubna, Russia, [4]Czech Academy of Sciences, Institute of Biophysics, Brno, Czech Republic, [5]German Cancer Research Center (DKFZ), Heidelberg, Germany

OPEN ACCESS

Edited by:
Yolanda Prezado,
INSERM U1021 Signalisation Normale et Pathologique de L'embryon aux ThÃ©rapies Innovantes des Cancers, France

Reviewed by:
Charlot Vandevoorde,
iThemba Laboratory, South Africa
Judith Reindl,
Munich University of the Federal Armed Forces, Germany

***Correspondence:**
Michael Hausmann
hausmann@kip.uni-heidelberg.de
Martin Falk
falk@ibp.cz

Specialty section:
This article was submitted to Medical Physics and Imaging, a section of the journal Frontiers in Physics

Received: 30 June 2020
Accepted: 22 September 2020
Published: 09 November 2020

Citation:
Hausmann M, Neitzel C, Bobkova E, Nagel D, Hofmann A, Chramko T, Smirnova E, Kopečná O, Pagáčová E, Boreyko A, Krasavin E, Falkova I, Heermann DW, Pilarczyk G, Hildenbrand G, Bestvater F and Falk M (2020) Single Molecule Localization Microscopy Analyses of DNA-Repair Foci and Clusters Detected Along Particle Damage Tracks. Front. Phys. 8:578662. doi: 10.3389/fphy.2020.578662

High-LET (Linear Energy Transfer) particle irradiation as being provided from heavy ion accelerator facilities has an increasing impact on bio-medical research and cancer treatment. Nevertheless, there are a lot of open questions concerning the understanding of damaging mechanisms and repair processes within the light of radio-sensitivity and thus, individualized medical applications. The three-dimensional architecture of genomes on the meso- and nano-scale acts in combination with epigenetic gene activation as an important player of gene regulation and fundamental biological processes such as DNA damage response and repair. So far only little is known about the impact of high-LET particles on the chromatin architecture along the passing track when they are "lumbering" through the cell nucleus. How does a cell nucleus manage such complex damages and re-organize the chromatin toward functionally intact units? Is there a radio-sensitivity related difference in this reaction? Here, we present some approaches to investigate spatial and topological parameters of chromatin to glimpse some aspects related to these questions. Two cell lines, a radio-resistant glioblastoma and a radio-sensitive fibroblast cell line, were used and irradiated by ^{15}N-ions in 90° and 10° radiation beam geometry. Nano-probing of particle induced damage sites along particle tracks, and the recruited DNA repair proteins (as presented here for 53BP1 and Rad51) in combination with super-resolution Single Molecule Localization Microscopy (SMLM) are powerful methods for geometric and topological analyses to study particle related mechanisms of chromatin conformation and repair complexes in single cells. We used variable tools for such investigations based on image free high precision SMLM, nano-scaled molecule distribution analyses, appropriate metrics following Ripley's distance frequencies and cluster formation analyses, as well as topological quantifications employing persistence homology. The data reveal a cell type specific nano-architecture of DNA damage foci along particle tracks and their dynamic molecular re-arrangements during repair. Comparing the topology of repair foci by persistence homology suggests similarities of repair cluster formation along given particle tracks. Our studies contribute to

the molecular understanding of cellular radiation response at sub-light microscopic chromatin levels; thereby showing how chromatin architecture around complex damage sites and repair foci nano-architecture may contribute to ongoing repair processing. The methodological approach presented here may give a basis for improved biological dosimetry or radiotherapies in the future.

Keywords: heavy ion irradiation, single molecule localization microscopy, Ripley distance frequency analysis, topological analysis, persistent homologies, ionizing radiation-induced foci, DNA double strand breaks

INTRODUCTION

All over the Universe, matter is subjected to extreme conditions as for instance high temperatures, pressures, and densities. Stellar collisions and explosions prepare ultra-fast heavy ions interacting with any material crossing their ways. With mankind´s quest to discover space and our planetary system not only by vehicles but also by manned space missions, an understanding of interactions of these heavy ions with biological and especially cellular systems has become an urgent demand to science [1]. Modern nuclear accelerators enable researchers to create radiation conditions of space in the earth-based laboratory. Particle beams of various elements at different intensities and qualities can be generated and applied on cells, tissues, organs or organisms. While protective systems to control or even to avoid accidental exposure of humans on space missions are under development [2, 3], targeted applications as for instance the powerful treatment tool against aggressive tumors especially brain tumors, have been established worldwide in medicine [4, 5].

Up to now research has delivered a huge amount of knowledge and findings of biological, epigenetic response to low-LET (Linear Energy Transfer) photon and high-LET particle irradiation; thereby a lot of questions concerning damaging profiles and repair response remain unanswered [6–10]. Scientific results improving the understanding of mechanisms behind damaging and repair are demanded in order to optimize space mission planning or to individualize radiation treatment [11]. Therefore not only defined radiation experiments in accelerator facilities are required but also novel tools to elucidate components of epigenetic control and their impact on radiation response.

Radiation induced DNA damages are depending on the dose, dose rate, LET, radiation type, cell radio-sensitivity, DNA repair capacity, etc. In contrast to low-LET photon irradiation which induces DNA damages in a coarse gain pattern, high-LET particles (e.g., protons, α-particles, heavy ions) pass the chromatin in linear tracks [12] along which a complex damaging process happens, which locally may lead to an overload of single (SSB) and double strand breaks (DSB) [13–15]. The most severe damages being created are complex double-stranded breaks (DSBs) of the DNA molecule [16]. These complex lesions consist of several SSBs and DSBs generated in close mutual proximity in combination with other types of DNA damages [17] and highly challenge all repair mechanisms being available for cellular survival [18–20]. Multiple complex DSBs often remain unrepaired which leads to cell death, the treatment effect envisaged in successful radiation cancer therapy.

On the other hand, escaping cell death, the complexity of lesions increases the risks of dysfunctional cells with mutations and chromosome aberrations, a serious problem, which medical radiation treatment schemes always have to avoid [21–23]. In contrast to cell death being required for heavy ion radiation therapy, radiation protection in the field of long-term space missions planned [2] should save the cells in their best functional conditions. These extremely opposite demands show the urgent need for further investigations in order to better understand the mechanisms of DNA damaging and repair.

In general, the genome is responding to DSBs by specific phosphorylation of histone H2AX in a 2 Mbp region surrounding the chromatin damage site, which can be visualized in form of so-called γH2AX foci [24, 25] against which specific antibodies are available. Inside these foci, the cell starts to repair the damage by recruiting and releasing a complex network of proteins along given repair pathways. The main repair pathways are the canonic non-homologous end-joining (c-NHEJ), the homologous recombination (HR) and the less precisely classified alternative (or backup) pathways, such as Ku-independent non-homologous end-joining (a-NHEJ), single-strand annealing (SSA) or microhomology-mediated end-joining (MMEJ) [26–30].

All these repair pathways are functioning differently and recruit different series and amounts of repair proteins to the initially induced γH2AX damage foci. The main differences in the chosen pathways are the speed and quality of repair. HR is very precise in maintaining the base sequence of the damaged region exactly; thereby it is slow since an appropriate DNA sequence template has to be arranged, the damaged sites have to be resected correctly, and nucleotide by nucleotide has to be reconstructed. In contrast to HR, c-NHEJ is fast but tolerates the loss of some nucleotides in the new strand after trimming and "sticking" the broken ends together. a-NHEJ and other alternative pathways only seem to play a significant role after multiple damaging by high dose exposure. Due to a lack of availability of enough repair proteins, broken ends are repaired under omitting some typical c-NHEJ proteins with the consequence of being slow and more error prone. Repair errors also occur due to illegitimate recombination between short homologous sequences or repeats.

At a first glimpse, it appears that a cell decides individually or even randomly which repair pathway is used at a given damage site. However, a more detailed view on repair processes reveals that repair pathway selection is depending on several conditions like the phase of the cell cycle, the chromatin structure and compaction at the site of damage, the complexity and multiplicity of DSBs, the general radiation sensitivity of the cell type, and potentially several other factors [19, 31–42]. All these factors

contributing to repair pathway choice at a given damage site in a given cell type require a complex epigenetic controlling system [9, 10] that may interact according to so far not fully understood rules.

Beyond the "classical" epigenetic systems following so far known epigenetic protein pathways, another level of epigenetic function and control appears to be relevant for further consideration especially in case of complex damaging processes. This epigenetic system, not pushed into the focus of investigations, yet, is the chromatin architecture. Chromatin architecture is known to be functionally organized [43, 44] on the micro-, meso- and nano-scale, and its relaxation and precisely regulated re-arrangements were observed at damage sites [6, 45]; reviewed in Ref. 8 [9, 10]. On the sub-micro scale, local chromatin architecture changes after DNA-damage induction and along repair processes. In the context of chromatin architecture, two perspectives have to be considered: a) the broken chromatin strands with their chemically different ends, environment of H2AX phosphorylation and variable mobility [6]; [8], and b) the spatial organization of repair protein during formation and release of repair complexes (visible as repair foci). Understanding how spatial arrangements of chromatin and recruited proteins impact DNA repair, requires a precise analysis of geometry and topology of single molecules of γH2AX as well as of by repair proteins forming foci, e.g., MRE11, 53BP1, RAD51, etc. Counting of these foci, generally known as Ionizing Radiation-Induced Foci (IRIFs), by means of light microscopy has become a well established measure for intra-cellular dosimetry [14, 46, 47]. Until recently, the investigations of nano-architecture of chromatin and repair complexes had to rely on electron microscopy [48–50], which, however, suffers from serious limitations and disadvantages. A breakthrough in the field was brought about by the development of super-resolution light microscopy techniques [51, 52], based on specific labeling of the target molecules that allowed to overcome Abbes' diffraction limit [15, 45, 53–56].

For low-LET radiation, the numbers of DSBs and labeled γH2AX foci are directly correlated, although it is still under debate whether and how many DSBs are joined together within one IRIF. For high-LET radiation, it has become obvious that foci are enlarged and their number is considerably below the predicted number of DSBs [14, 57, 58]. This phenomenon can be explained by overlapping and aggregation of several foci in a not well defined way. The internal architecture and complexity of repair foci after high-LET particle traversing, however, have not been systematically and thus satisfyingly investigated. The spatial structure, organization, and topology of IRIF thus remain to be intensively discussed. Open questions such as the arrangement of elementary or functional foci sub-units call for further research on the nature and typical parameters (shape, size, quantitative composition, etc.) of these still mysterious structures and their relationship to particular repair pathways.

Investigations using super-resolution light microscopy or electron microscopy revealed sub-structures like clusters within γH2AX or repair protein (e.g., 53BP1, MRE11, Rad51, pATM etc.) foci. These cluster can be observed independently of nature or the LET of radiation [49, 54, 56, 59–65]. For low-LET irradiation, the number of repair-focus sub-units (clusters) seems to better correlate with the number of DSBs and damage complexity than the number of IRIFs detected at the microscale [54]. In addition, after low-LET irradiation, γH2AX cluster sub-units were found to show high topological similarity provided they were closely associated to heterochromatin [66].

For high-LET irradiation, beyond the analyses of γH2AX foci and sub-units [15, 16], it has become obvious that the architecture and topology of the clusters of the follow-up recruited repair proteins is important with respect to the question of spatial organization of molecules as epigenetic control systems. 53BP1 foci were analyzed in more detail [15, 55, 56] after high-LET radiation exposure. 53BP1 is involved in NHEJ and acts as a stabilizing factor during HR [67]. 53BP1 binds to methylated regions of histones where it interacts with other repair proteins, for instance to promote NHEJ. During such interactions, 53BP1 could be displaced from the primary damaged sites [68, 69] opening them for instance for access of BRCA1 or CtIP.

SMLM [70, 71] has been successfully applied to study DNA repair and cluster formation of γH2AX molecules under low-LET radiation condition [53, 54, 72] and during long-term cell culture under folate deficiency [73]. Foci and sub-focus clusters of repair proteins were also investigated after particle irradiation [15, 55, 56].

SMLM of fluorescently tagged 53BP1 molecules was performed and clusters of these tags were determined as sub-units of repair foci, so that the formation and relaxation of these clusters could be studied during the repair period [15, 55].

In the article presented here, we continue in the analysis of 53BP1 clustering after ^{15}N particle irradiation with the focus on cluster size and environment during repair. In addition, we will show that persistent homologies of clusters as being calculated by topological methods of mathematics show different degrees of similarities in cell lines of high and low radio-sensitivity. These tools exemplarily presented here may be used to classify foci with respect of their follow-up repair mechanisms. Nitrogen ions were used as they are relevant for both space research and radiotherapy. They are present in galactic and solar cosmic radiation [74] and are extensively produced when cosmic radiation interacts with the atmosphere [75]. Interestingly, Pioneer 10 spacecraft have revealed increased (up to the factor of 20) amounts of N (and O) ions relative to their abundance in galactic or solar cosmic rays, pointing to specific sources of this component of cosmic radiation in the Universe [76]. N-ions are also generated during hadron radiation therapy and may significantly contribute to the patients' absorbed dose [77]. Nitrogen ion beams have been also studied as promising particles for radiotherapy [78].

MATERIALS AND METHODS

Cell Culture and Specimen Preparation

Cell culturing and specimen preparation has been described in detail elsewhere [14, 15, 55]. In brief: Primary neonatal human dermal fibroblasts (NHDF) and human U87 glioblastoma cells

TABLE 1 | Radiation values of the experiments.

Irradiation angle	Dose [Gy]	Energy [MeV/n]	LET [keV/μm]	Fluence [10^6/cm] per 1 Gy	Expected Mean Number of Particles/Nucleus
10°	1.3	13.1	181.4	3.40	2.1
90°	4.0	13.0	182.9	3.41	25.4

were cultured in Dulbecco's modified Eagle medium (DMEM) supplemented with 10% fetal calf serum (FCS) and a 1% gentamicin-glutamine solution (all reagents from Sigma-Aldrich). For the ion-radiation experiments, the cells were maintained in T 25 cell flasks at 37 °C in a humidified atmosphere with 5% CO_2. 16 – 18 h before irradiation, cells were seeded on glass coverslips fixed on bottoms of Petri dishes and cultivated until 80% confluence. The cells were irradiated at room temperature. After irradiation the samples were further cultivated and individual slides in duplicates were fixed with 4% formaldehyde/PBS (phosphate-buffered saline) at indicated periods of times post-irradiation (PI), ranging from 5 min PI to 24 h PI (5, 15 min (10° only), 30, 45 min (10° only), 1, 2, 4, 8, 24 h). This approach ensured that cells of the same condition (proliferation phase, cell cycle distribution, and physiological status) were analyzed at all post irradiation time point. For fluorescence labeling, the cells were washed twice in 1x PBS, permeabilized in 0.2% Triton X-100 at RT, washed again three times in 1× PBS, and incubated in 2% bovine serum albumin (BSA) for 60 min at RT. Primarily rabbit anti-53BP1 (ab21083, Abcam) antibodies or rabbit anti-Rad51 (ab63801, Abcam) antibodies, respectively, were added to the cells and the cells were rinsed with 0.2% Triton X-100 and washed three times with 1× PBS for 5 min at RT. The secondary antibodies, AlexaFluor 594-conjugated goat anti-rabbit (Johnson Laboratories) (53BP1), or Alexa Fluor 568-conjugated donkey anti-rabbit (ThermoFisher Scientific) (Rad51), respectively, were applied to the cells for 30 min and again the cells were washed three times in 1× PBS for 5 min and counterstained with DAPI. After washing the slides three times in 1× PBS for 5 min each, the cover slips were air dried, and the cells were embedded in ProLong Gold® (ThermoFisher Scientific) for SMLM. Prolong Gold was left to polymerize for 24 h in the dark at RT before the slides were sealed with nail polish and stored.

Specimen Irradiation

As described in detail elsewhere [14] ^{15}N ions were accelerated using a U 400M isochronous cyclotron in the Flerov Laboratory of Nuclear Reaction at the Joint Institute for Nuclear Research (JINR, Dubna) [79]. The radiation conditions applied are summarized in **Table 1**.

In the experiments, cells were exposed to an average of about 2 and 25 particles per nucleus for 10° and 90° irradiation, respectively. This corresponds to the doses of 1.3 Gy (10° irradiation) and 4.0 Gy (90° irradiation). The values were calculated as described in Ref. 80; for the average nuclear area of 186 μm^2. The non-homogeneity within the irradiation field of 14 mm in diameter was less than 5%, as monitored using five identical flow-type ionization chambers; the central chamber served as the monitor of the radiation dose [79]. The energy and corresponding LET values of ions at the plane of the cell monolayer were calculated using LISE++ software [81].

The cells were irradiated on glass coverslips at Petri dish bottoms tangentially or perpendicularly. The side of the coverslips covered with cells was oriented toward the ion beam so that the cells were hit by the particles before the beam entered the culture medium in the Petri dish. During irradiation, the cells were kept in a thermostable box, ensuring a constant temperature of 37 °C and prevention from infection during the whole procedure. After irradiation, the cells were immediately placed back into the incubator until fixation. For microscopic analyses, the cell nuclei were fixed at numerous periods of time after irradiation (5 min–24 h PI), as explained in detail in paragraph *Cell Culture and Specimen Preparation*.

Single Molecule Localization Microscopy

A detailed description of the SMLM instrument has been published elsewhere [53, 54, 64, 82]. In brief: The microscope has an oil-objective (100×/NA 1.46) and four lasers 405 nm/491 nm, respectively. Measurements were done with the 561 nm wavelength laser. An in-built electron multiplier (EM-gain) enhances signals detected by the EmCCD camera (80 nm/px). The microscope was installed on a Smart-Table compensating for vibrations, and provided with a water-cooling system to keep constant temperature and to minimize drifts. Lasers were controlled using the "Omicron Control Center" program and image acquisition was carried out using "Live Acquisition v. 2.6.0.14" software. For thermal stabilization, first measurements with the microscope were performed 1 h after booting.

A protocol for automatized localization image acquisition was used. In brief, an initial excitation switched most fluorophores into a reversibly bleached state; then 2,000 single image frames were taken at maximum laser power with an exposure time of 100 ms per image frame. Wide-field images were always taken before localization image acquisition. For each time point during the repair period, a minimum of 23 cells was imaged. The image data stacks were stored as *.tif stacks and subjected to further computational analysis as described below.

Data Evaluation and Image Processing

The local positions of the detected dye molecules of the antibodies were obtained from registration of molecular blinking events according to an algorithm described elsewhere [82], which is based on subtraction of the brightness values of two successive frames. This method enables the differentiation of the blinking events from the background. A so-called "Orte-Matrix" was produced, which contained information about the signal

TABLE 2 | Cluster parameters of the experiment.

cluster values	53BP1				Rad51	
Cell line	NHDF	U87	NHDF	U87	NHDF	U87
Irradiation angle	*10°*	*10°*	*90°*	*90°*	*10°*	*10°*
Radius [nm]	200	200	200	200	200	200
Min Number of points	65	65	84	55	60	60

amplitude, the lateral x- and y-coordinates, the standard deviations in the *x*- and *y*-direction, position errors, etc. This "Orte-Matrix" was the starting data set for all further evaluation procedures and for the construction of artificial images of the cell nuclei.

Mathematical procedures and algorithms were applied on these raw coordinate data of the detected labeling points instead on processed images. The data analysis program is modularly built up and was programmed in Python (https://www.python.org) (Gote, Neitzel et al., manuscript in preparation). Several algorithms developed are based on Ripley's point-to-point distance frequency measure structure information [84] or use DBSCAN [85]) in order to obtain information whether the fluorophores were localized in clusters. The point-to-point distances were measured by distances from each given central point to its peripheral ones. Without regarding absolute position information, the graphical display of absolute and relative distance frequencies makes it possible to discriminate between specimen structure signals and background signals. The envelope function of the distance frequency histogram is correlating to functional arrangements of points [53].

A homogeneous point-to-point distance distribution leads to a linear increase in the distance frequency histogram. The slope of the straight line is scaled with the number of detected points. If the points appear in clusters, smaller distances are more frequent resulting in a peak. The width of the peak gives the maximum distance between two points in the cluster and thus the cluster diameter. The area under the peak is a measure relative to the point density in a cluster. The shape of the peak gives a measure of the homogeneity of the distribution of points in the cluster. If clusters are embedded in a pointillist background, the result consists of three parts: a) a homogeneous distribution (linear increase); b) a cluster distribution (peak) and c) a cross term or additional peak, which contains the distances between the points of two neighboring clusters.

According to the DBSCAN algorithm [85], clusters are compact regions of increased local density of points. The amount of all points inside a given radius around a point must have a minimum value to define a cluster. If any points inside such a cluster also meet the cluster definition they are attributed to the same cluster. The cluster size is the maximum area in which all points meet the cluster criteria. Inside clusters various characteristics can be examined and compared to the point distributions outside the clusters.

The following cluster parameters describing the minimum number of points within a given radius were interactively determined (**Table 2**).

Novel analytical methods for 53BP1 cluster characterization were applied using procedures of persistence homology [66]. This method, using established calculations and mathematical operations, allows two point distributions, here the point distributions of 53BP1 clusters of two irradiation schemes, to be compared to each other in a cell-independent manner, thereby giving a mathematical measure of their similarity [86].

The major principle of this analysis for persistent topologies is to record properties of point patterns, which are invariant under certain deformations of the object. Mathematically these deformations correspond to continuous transformations of the topological space defined by the structures. For 53BP1 clusters, the attention was focused on two properties: a) the number of "components", which are independent from each other in such sense that connections between points only exist within the respective components; b) the number of "holes" of the structures inside the components. In algebraic topology, these properties are called the Betti numbers for zero- and one-dimensional simplicial complexes. They are the topological invariants that distinguish between different topological spaces.

SMLM data sets of repair foci are clustered point-sets for which components and holes can be defined [66]. In the following, this procedure is briefly described: A geometric relationship among cluster points is obtained by growing spheres of radius α around each point. Whenever two of these spheres mutually embed each-other's center, these centers are connected by a line. The connected points belong to the same component. With increasing radii of the spheres, more and more points are connected to previously disjoint components. Thus, the number of components is decreasing with increasing of the radius α. At the end of the procedure, a single component is remaining. For the definition of holes, the simplest polygon, the triangle, is appropriate. Whenever a component of three connecting lines of points forms a triangle, the area of the triangle is considered as a hole. With reducing the number of disjunct components, the number of holes is increasing and decreasing again.

The amounts of components and holes are depending on the value of α. For the formation of each component and each hole, a bar of a barcode pattern starts. The end of the respective bar is fixed at the disappearance of components and holes with increasing α [87]. The mathematical transfer of the spatially organized pattern of labeling points into barcodes contains information about components and holes in a compact and illustrative way. The sets of barcodes for each 53BP1 cluster were compared with each other and their similarity was calculated. The procedure used for quantification of the barcodes similarity is based on the Jaccard index [88]. A detailed description and illustration is presented in Refs. 66 and 86. The result of this normalized similarity measure is a value between 0 and 1, where a value of 0 means no overlap of two bars and 1 the identity of two bars. The similarity of barcodes of different dimensions is defined as the average of the individual similarity values of the bars of a cluster. Such topological comparisons are independent of the scale and the perspective on the clusters so that it is possible to compare variably large foci randomly orientated to the microscopic detection system.

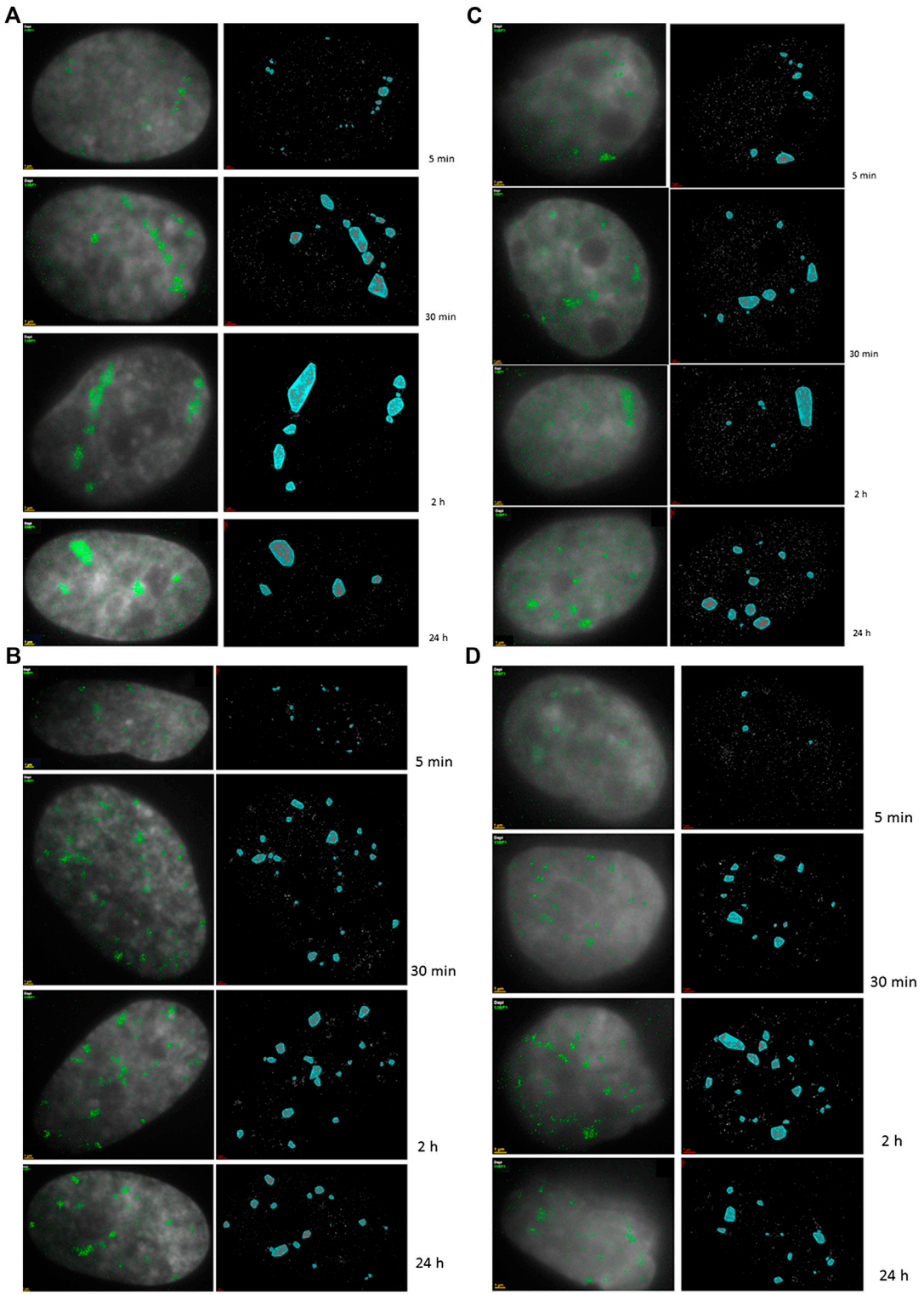

FIGURE 1 | 2D density SMLM images of 53BP1 repair proteins. Typical examples are shown for fluorescently-labelled 53BP1 proteins in NHDF cells **(A,B)** and U87 cells **(C,D)** after 1.3 Gy tangential ^{15}N-irradiation **(A,C)** (10° angle between the ion beam and the cell layer) and 4 Gy perpendicular ^{15}N-irradiation **(B,D)** (90° angle between the ion beam and the cell layer). The time values indicate the period PI when the samples were taken as aliquots of the same irradiated culture and fixed. For comparison, examples of non-irradiated control cells are presented. The left columns are merged images of SMLM data and wide-field images. In the right columns the SMLM image data and cluster areas are shown. The scale bars equal to 1 μm.

RESULTS

The Neonatal Human Dermal Fibroblast (NHDF) line was studied as model of normal (non-transformed) cells with relatively higher radio-sensitivity while U87 glioblastoma cells were selected for their high radio-resistance [55] and aggressive cancer phenotype. In addition, forming the skin, NHDF fibroblasts are always irradiated by external radiation sources. Glioblastoma (U87 cells) then represents a tumor treated by radiation but with poor results only due to its high radio-resistance. Both cell types were exposed to high-LET ^{15}N ions in two different geometries (i.e., under the angle of 10°and 90° as described in *Materials and Methods*) and IRIF formed by γH2AX and selected repair proteins (53BP1 and Rad51) were studied with SMLM in different periods of time post-irradiation (PI), ranging from 5 min PI to 24 h PI. Within the first minutes after irradiation, 53BP1 proteins were recruited to the damaged sites, visualized as γH2AX foci. 53BP1 foci provide information of the early recruitment of proteins for repair. In the previous studies [15, 55], we have shown that DSB repair proceeds much slower in cells exposed to (high-LET) ^{15}N ions than in cells irradiated with low-LET γ-rays. Also, it emerged obvious that 53BP1 repair foci differ in their parameters for NHDF and U87 cells. Here, the 53BP1 data sets already investigated by SMLM [55] were further analyzed for structural clustering and topological similarity. In addition, data sets of the same cell types and radiation conditions were prepared also for Rad51 protein, which is, unlike 53BP1, selectively involved in DSB repair via homologous recombination. The first data of Rad51 labeling and spatial organization of Rad51 foci were elucidated and compared to results obtained for 53BP1 repair protein participating both in NHEJ and HR. Focus formation and clustering, persistent homologies, and structural changes during the post-irradiation (PI) period of repair were analyzed at several repair relevant time points (5, 15 min (10° only), 30, 45 min (10° only), 1, 2, 4, 8, 24 h).

In contrast to U87 cells, NHDF fibroblasts quickly recruited the majority of the 53BP1 proteins (~60%) to the damaged chromatin sites along the particle tracks so that clusters have already been visible and well developed at 5 min PI, though their number progressively increased within the first 30 min PI. In both cell types, the cluster numbers were maintained until 8 h and then started to decrease; thereby a considerable proportion of clusters persisted even after 24 h PI (**Figure 1**).

U87 cells contained 53BP1 clusters also prior to irradiation (control samples) which was not observed in NDHF cells. In U87 cells, the formation of 53BP1 clusters in tracks was delayed up to 30 min PI and the relative number of recruited 53BP1 proteins was always less than 40% of the protein pool available. These results thus confirmed our previous observations [55]. In **Figure 1**, illustrative examples of SMLM images of 53BP1 foci/clusters are shown for the two cell lines, the two radiation schemes, and different periods PI. The left images show wide-field images of DAPI-stained nuclei with inserted point signals of individual 53BP1 molecules acquired with SMLM. The right columns then provide the corresponding SMLM images of the 53BP1 foci after cluster area determination. For the 10° irradiation angle, the specimens of both cell lines showed characteristic tracks highlighted by dense arrangements of labeling tags. At later periods PI, the tracks partly dissolved and separated protein cluster units became visible dispersed, over the cell nuclei. In contrast to the 10° irradiation experiments, the 90° irradiation experiments showed more clusters irregularly dispersed over the cell nucleus. Since the dose was higher in these experiments, all these clusters may represent a separate particle track perpendicular to the image plain.

The following investigations are reasoned by the hypothesis that repair proteins form characteristic, similarly sized clusters at the damaged chromatin sites. These proteins are recruited to and released from clusters during the repair period; thereby their spatial topology can be expected to show high similarity provided the chromatin environment around the damage sites is also similar and the same repair mechanism has been activated. The correct topological arrangement is assumed to be required for the downstream repair steps so that the follow-up repair protein molecules could correctly access the damaged chromatin sites. The results presented here support these ideas and show by which mathematical operations the biophysical verification of the hypothesis could be approached.

To further investigate the dynamics and cluster formation of tagged 53BP1 molecules, Ripley distance analysis was applied that is based on relative frequency histograms of pairwise point distances. The distance frequency histograms were compared for all repair time points of each cell type and each radiation condition. In **Figure 2**, the results are presented. The controls of both cell lines showed a peak at smaller distances, which indicates these small distances occur very frequently, i.e., the labeled proteins are often arranged in such closely adjacent conformations (=cluster conformations). These clusters are embedded in a random distribution of points which can be concluded from the linearly increasing frequency of larger distances. Note that the histograms show the relative frequency of distances but do not give information about the absolute number of distances or clusters.

Shortly after irradiation, the formation of clusters increases in NHDF cells but not in U87 cells. Subsequently, from 1 h PI, the absolute cluster frequency was decreasing in NHDF cells. For longer periods PI (2–24 h), some clusters remained while the rest of protein labeling points followed a strong random distribution (**Figures 2A,B**). This behavior was found for both, the 10° and 90° irradiation schemes, though it was less pronounced for 90° (compare **Figure 2A** vs. **2B**).

The cluster and labeling point dynamics appeared to be different in U87 cell nuclei (**Figures 2C,D**). Significant clusters were found also in the non-irradiated controls, embedded within a random labeling point pattern. For the 10° irradiation scheme, the amount of labeling points was increasing and larger clusters were formed after 5 min PI (**Figure 2C**). From 15 min PI until the end of the period of investigation (24 h), the clusters kept their size and remained. Some minor fluctuations within some randomly dispersed labeling points were observed. For the 90° irradiation scheme, the control showed the same behavior as for the 10° irradiation scheme, separate clusters within an

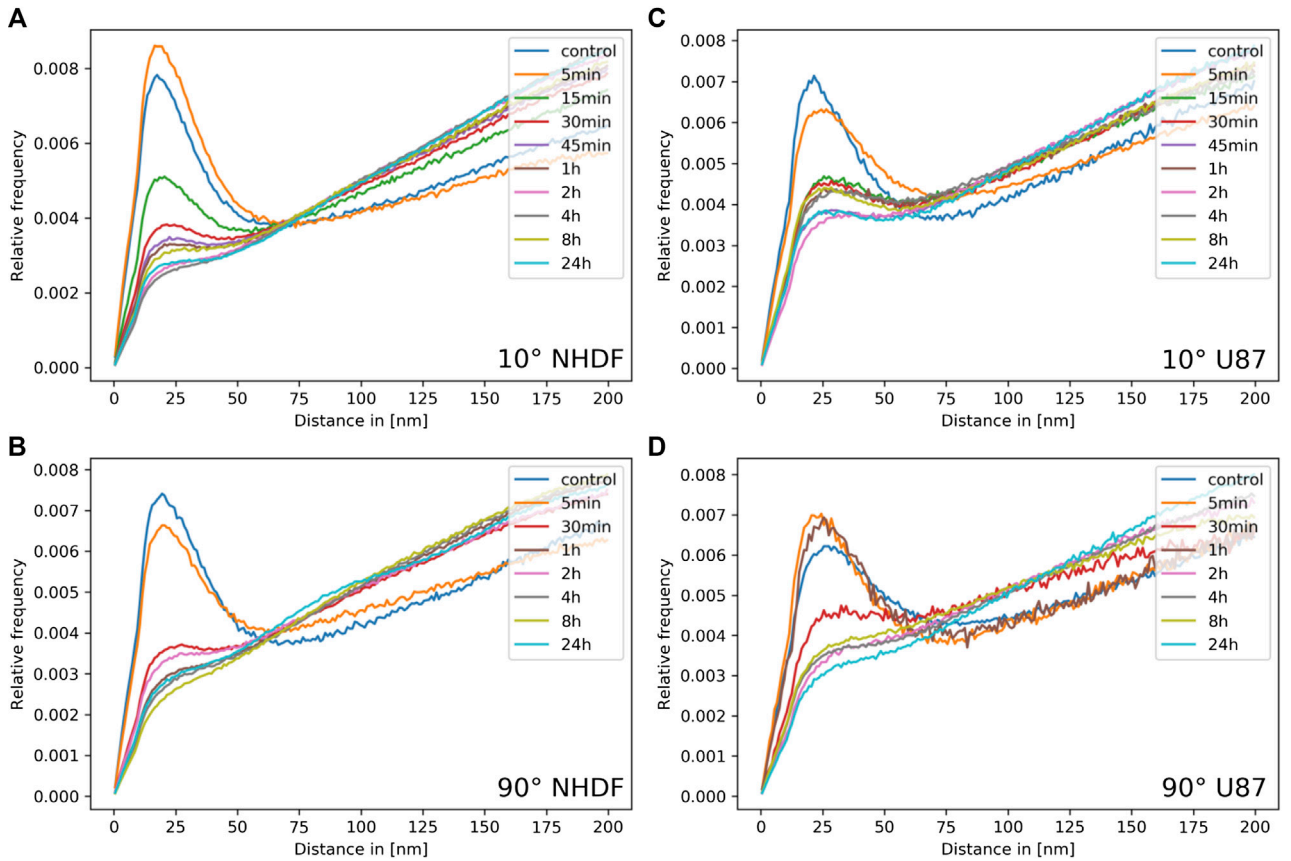

FIGURE 2 | Ripley distance frequency analysis. The relative frequencies of pairwise distances are presented for the aliquots of the irradiated cell samples at different time points PI (color label of curves); **(A)** NHDF and **(C)** U87cells irradiated under 10° irradiation angle; **(B)** NHDF and **(D)** U87cells irradiated under 90° irradiation angle.

TABLE 3 | Overview of the number of clusters included into the analyses of persistent homologies.

	NHDF, 10°	NHDF, 90°	U87, 10°	U87, 90°
Number of clusters evaluated	198	297	146	219

environment of randomly dispersed labeling points. However, after irradiation with the high dose (4 Gy), the situation was different as fluctuations in cluster formation and size appeared until 2 h PI (**Figure 2D**). Between 2 and 24 h PI, a low clustering frequency within a strong random distribution of labeling points could be seen.

These measurements, in conclusion, indicate that 53BP1 clusters are quickly formed after irradiation. With the progress of the early repair period (ending at about 30 min or 1 h PI) one part of the clusters becomes dispersed while the other part persists within a growing amount of randomly distributed proteins. These persistent clusters remained in cell nuclei until the end of the investigation period (24 h PI).

In the next step, we decided to analyze "remaining" 53BP1 clusters at 2 h PI in terms of the persistent homology and determined the degree of their mutual topological similarity. Based on the pointillist information obtained by SMLM, we used this new analytical method for 53BP1 cluster characterization after high-LET ^{15}N ion irradiation for the first time. A cell independent, pairwise comparison of point distributions (here the point distributions of two 53BP1 clusters) with each other was elaborated for a selected ensample of clusters. For the evaluation, the following total numbers of clusters were considered (**Table 3**):

The resulting barcodes of 0 (components) and 1 (holes) dimensions were compared in both directions and a mathematical measure of their similarity was calculated and visualized in heatmap descriptions (**Figure 3**). For both cell types the similarity measure as being determined by the Jaccard index was very high for the components (>0.9) independent of the irradiation scheme (**Figures 3A,B, a**). This indicates that the complex, ion-induced damages are marked with a specific repair cluster setup. On the other hand the similarity measure for the holes was below 0.5 for both cell types and radiations schemes (**Figures 3A,B, b**). Interestingly the similarity of holes was on average higher for NHDF (**Figure 3A, b**) than for U87 cells (**Figure 3B, b**).

The similarity values obtained by averaging of components and holes values for each 53BP1 cluster are presented in **Figures 3A,B, c**. When the clusters of the 10° irradiations scheme were

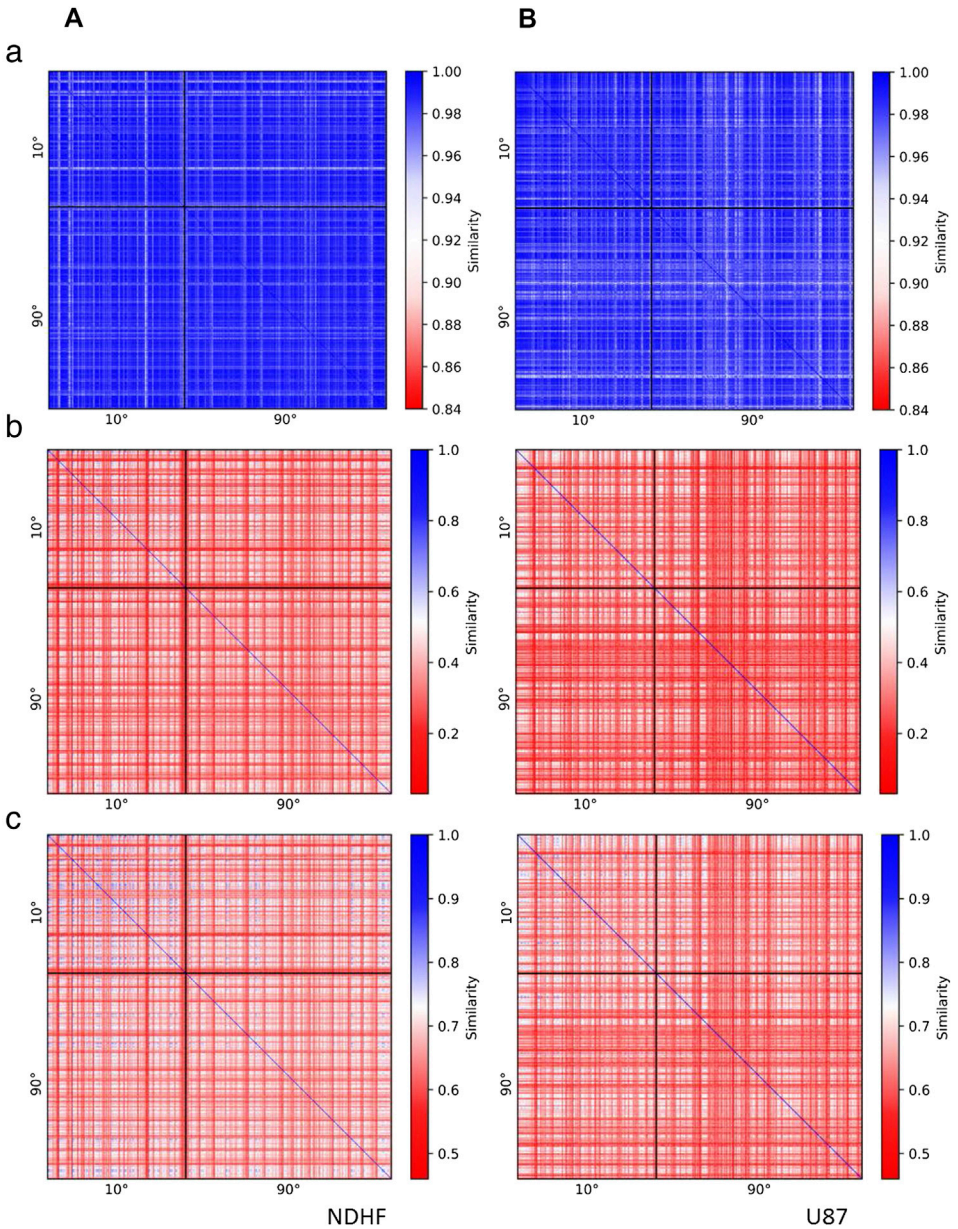

FIGURE 3 | Heatmaps indicating the similarity of 53BP1 clusters in **(A)** NHDF cells and **(B)** U87 cells irradiated under an irradiation angle of 10° or 90° and fixed 2 h PI. The heatmaps show **(a)** the similarity of the barcodes of dimension 0 (components), **(b)** the similarity of the barcodes of dimension 1 (holes), **(c)** the average similarity of the barcodes of dimension 0 and 1. The comparison of clusters in cells irradiated with 10° (90°) is shown in the upper left (lower right) corner of the heatmaps. In the upper right (lower left) corner clusters in cells irradiated with 10° (90°) are compared to clusters in cells irradiated with 90° (10°). Clusters occurring in the same cell are located next to each other in the heatmap. Blue color indicates that the compared clusters have similar topological characteristics, whereas red color indicates differing cluster characteristics.

compared, the Jaccard indices laid between 0.55 and 0.82 for both cell types. The frequency distribution was broad without a peak for NHDF cells whereas U87 showed a clear peak at 0.64 (**Figure 4**). Comparing the clusters of the 90° irradiation scheme, the peak was at 0.63 for U87 cells. This value was also obtained for the comparison of the 10° with the 90° irradiation scheme. For these two comparisons (90° vs. 90°, 10° vs. 90°), NHDF cells showed a bimodal peak distribution with one peak at 0.67 and another peak at 0.72 (**Figure 4**). In general it can be concluded that the more radio-sensitive NHDF cells revealed a higher topological similarity in 53BP1 clustering than the more radio-resistant U87 cells.

53BP1 is known to be preferentially involved in NHEJ but it could also act as a stabilizing factor during HR. So in a very first approach we wanted to see whether under harsh damaging conditions occurring during high-LET ion irradiation, HR is

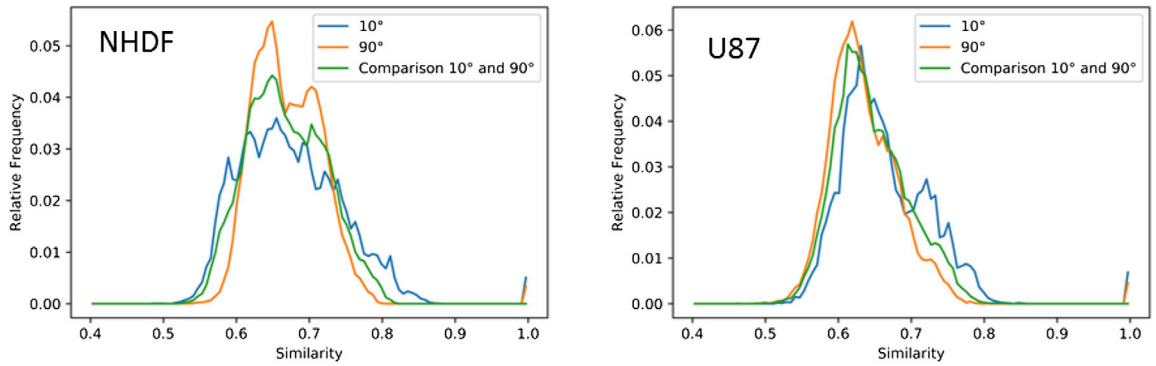

FIGURE 4 | Normalized histograms of the frequencies of similarity values of barcodes (Jaccard indices) of 53BP1 clusters in NHDF and U87 cells irradiated under 10° or 90° irradiation angle and fixed 2 h PI. The distributions of the average similarity of dimension 0 and 1 barcodes of 53BP1 clusters in NHDF (compare **Figure 3A,c**) and U87 (Compare **Figure 3B,c**) cells are shown. The similarity distributions of clusters in cells irradiated under an angle of 10° (values from the upper left part of the heatmaps) are shown in blue, the similarity distributions of clusters in cells irradiated under 90° (values of the lower right part of the heatmaps) are shown in orange, and the similarity distributions obtained when comparing clusters in cells irradiated with 10° to clusters in cells irradiated with 90° (values of the upper right part of the heatmap) are depicted in green.

used for DNA damage repair. Therefore we labeled γH2AX and Rad51 simultaneously in cell nuclei of the two cell lines under the 10° irradiation scheme. In **Figure 5A**, a typical example is shown. It was obvious that also HR was employed as a repair pathway for broken chromatin in the track. In these cases, the Rad51 signals were always completely embedded in a γH2AX environment. However, the frequency of Rad51 clusters was very different for the cells analyzed. For both cell types, nearly no Rad51 cluster was found in the control. An increase of Rad51 clusters emerged between 1 and 8 h PI for NHDF and between 2 and 8 h PI for U87. The number of Rad51 clusters at 24 h PI was again on the level of the non-irradiated control specimen (**Figure 5B**).

DISCUSSION

High-LET particle radiation has a Janus-faced nature. On one side it is highly dangerous and risky, as for instance during space mission. Even single particles could have a significant damaging effect on individual cells, with an unpredictable outcome for astronauts on space missions. On the other hand, high-LET particles can inactivate cells deeply inside the patients' bodies, making them an ideal tool for radiation treatment, especially of brain tumors or tumors embedded in very sensitive (and potentially vital) tissues. Therefore radio-protection as well as radio-therapy require a better understanding of the processes which the cells employ to repair complex damage events along the particle track.

Heavy ion accelerator facilities offer defined high-LET radiation conditions as for instance in terms of the particle type, dose, irradiation angle etc. Hence, particle accelerators allow precise and defined experiments on given cell models, which are a prerequisite for sophisticated systematic analyses of DNA damaging and repair upon specific irradiation conditions. Research opportunities offered by these facilities have therefore rocketed bio-medical research.

High-LET particles lumbering through the chromatin of a cell nucleus induce a very complex damage pattern highlighted by γH2AX foci and other foci of recruited repair proteins. So far it is neither known how many damaged sites associate and are eventually repaired within one focus (visible at the microscale), nor whether the foci have an internal nano-structure composed of smaller sub-units (clusters), representing a single damage each, which are potentially functionally organized. A correct repair of the associated broken DNA ends indicates that the relevant repair units may be smaller clusters, for some reason aggregated in foci. Otherwise, multiple damage concentrated within one repair focus, would promote miss-repair in a much higher extent than it is observed. Hence, it cannot be excluded that the hypotheses of "repair factories", postulated but not confirmed to explain DSB repair and formation of chromosomal aberrations at the microscale (reviewed in Ref. 8), will be revitalized at the nanoscale. Therefore, it is of high interest to better understand the spatial organization of repair foci and consequently the repair mechanism resulting from defined spatial arrangements of repair protein clusters. This has motivated us to perform sophisticated microscopy studies of repair protein foci along particle damage tracks by means of super-resolution SMLM. Systematic investigations have been started using the radiation facility at JINR Institute (Dubna, Russia) by applying different doses of various high-LET particle radiation types at different doses and under different irradiation angles to well established cell systems of different radio-sensitivity. In Ref. 55; we analyzed the abundance and recruitment dynamics of 53BP1 repair protein, which indicated significant differences in IRIF nano-architecture between radiosensitive normal fibroblasts (NHDF) and cancerous, highly radioresistant U87 cells. Here, we have continued these studies with a special focus on cluster formation and topological cluster similarity. Ripley distance frequency analysis in combination with calculations of similarity values after evaluation of persistent homology provided novel insights

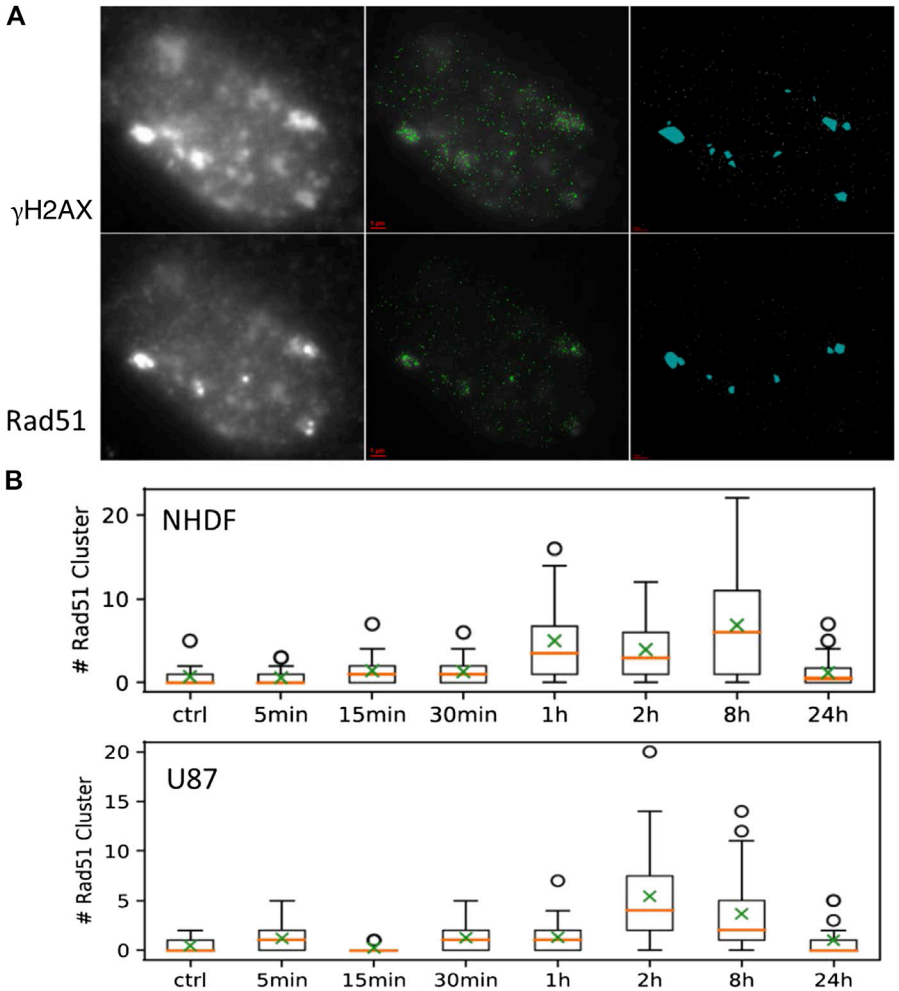

FIGURE 5 | (A) Example of an NHDF cell nucleus taken from the sample 1 h PI (irradiation angle 10°). Left: wide-field overview images taken in the color plain of γH2AX (upper row) and Rad51 (lower row); middle: SMLM image of the protein loci merged with the wide-field image; right: identified clusters as detected by the DBSCAN algorithm. **(B)** Box plots for the numbers of Rad51 clusters for NHDF and U87 cells determined in aliquots at different time points PI.

into the nano-architecture of repair foci that form at damaged sites in different cell types.

For normal NHDF fibroblasts, our data on 53BP1 molecules within IRIF revealed cluster formation and relaxation that was comparable for the two different radiations schemes and doses applied. In contrast, U87 cells showed a more variable cluster formation with fluctuations during the repair time. Moreover, independently of dose and irradiation angle the topology of the clusters was highly similar for NHDF cells in comparison to U87 cells. The high topological similarity of 53BP1 clusters in NHDF may indicate that, for both applied irradiation schemes, the 53BP1 clusters forming along the ion-induced chromatin damage have a specific, thus potentially functional setup. One reason for the existence of this setup may be the presence of several complex damage sites within the clusters instead of one single DSB. Further, with 53BP1 being located in the perichromatin and interchromatin [61], the specific arrangement of 53BP1 may be caused by the chromatin structure. Similar to our findings, the presence of resembling substructures of 53BP1 foci has also been observed by Reindl et al., who found that 53BP1 foci are subdivided into nano-foci of a constant size, thence no difference was observable in the setup of the nano-foci after low-LET proton and high-LET carbon ion irradiation [63, 89].

In addition, the comparison of the two cell lines (NHDF and U87) indicated that the loss of radio-sensitivity may be associated with a reduction of topological similarity of 53BP1 clusters. One possible explanation for this may be that, due to defects in DNA damage repair, U87 cells fail to build up clusters in a standard structured manner. In that case, the increased radio-resistance may originate from a "radiation adaptation" leading to cell survival with an unrepaired genome instead of more efficient repair [53]. As cancer cells often have modifications in their chromatin structure, another option would be that the characteristics in the repair cluster setup of U87 cells and their increased radio-resistance may be associated with chromatin re-

arrangements characteristic for carcinogenesis in general or specifically for this cell type. Nevertheless, a combination of several phenomena seems to be the most probable explanation. In Ref. 55; we observed that the more complex 53BP1 clusters disappeared much faster from U87 cells compared to NHDF fibroblasts though the overall repair kinetics of both cell types was more similar. This could mean that while some repair pathways are defective, the others are augmented.

Here, we wanted to introduce novel technical and mathematical approaches. The results of 53BP1 SMLM analysis revealed the potential of these proposed approaches. Future investigations will therefore be directed not only to further analyses of the clustering and topological similarity of 53BP1 at other time points PI but also to systematic investigations on γH2AX foci that directly indicate the reaction of chromatin to (low-LET vs. high-LET) radiation damage.

In general, the structure of the chromatin and the arrangement of proteins involved in repair may influence repair process and even the pathway choice by determining the accessibility of the damage site for follow-up proteins [55, 66, 90]. It has been proposed that 53BP1 is excluded from the center of the repair region and relocated to the outer part, if the DSB repair is directed to HR. This reposition opens space for loading of particular HR proteins, such as Rad51 [63, 67, 69, 91]. Hence, the structure of 53BP1 clusters may have a direct impact on the pathway selection. This correlation remains to be studied in future. As the first attempt to investigate the relationship between a specific topology of 53BP1 clusters, chromatin architecture at the damage sites, and initiation of HR, we have checked whether the HR marker, Rad51, is recruited to the damage track. In order not to find a Rad51 cluster or focus just by chance somewhere in the nucleus, we irradiated the cells in a sharp (10°) angle, which allowed us to visualize particle tracks trough the nucleus (using γH2AX as the damage marker) in the x-y plane of the microscope with much better resolution compared to 90° irradiation [14]. Indeed, during later repair times we found a considerable increase of Rad51 clusters that colocalized with γH2AX, indicating an increase in HR activity. This may be surprising since the harsh complex damage generated by high-LET particles could be expected to be a very challenging target for HR. On the other hand there seems to be special chromatin conditions that favor HR repair at high-LET damage sites. So far this data on the repair pathway selection at specific DSB sites are preliminary but indicate the need of further investigations in order to better understand how chromatin architecture affects chromatin functionality in relation to DNA damage repair. As presented here, powerful mathematical procedures applicable to SMLM data of repair processes are available that will shed new light into the shadow of complex damage events along particle tracks. As well, modern particle accelerators offer systematic evaluation of damage events induced by different types of precisely defined high-LET particle radiation.

DATA AVAILABILITY STATEMENT

All datasets presented in this study are included in the article.

AUTHOR CONTRIBUTIONS

Conceptualization, MH and MF; methodology, MH, MF, and AH; software, CN and AH; validation, CN, EB, DN, IF; formal analysis, CN, EB, DN, XX; investigation, CN, EB, DN, TC, ES, OK, EP; resources, AB, EK, FB, MH; data curation, CN, EB; writing—original draft preparation, MH; writing—review and editing, MF, CN; visualization, CH.; Supervision, MH, GP, GH, EK, DH, MF; project administration, MH, MF; funding acquisition, MH, MF. All authors have read and agreed to the published version of the manuscript.

FUNDING

The work was supported by the Czech Science Foundation (projects GACR 20-04109J and GACR 19-09212S to MF, by the Deutsche Forschungsgemeinschaft (DFG) grant (H1601/16-1) to MH, by the Heidelberg University Mobility Grant for International Research Cooperation within the excellence initiative II of the Deutsche Forschungsgemeinschaft (DFG) to MH, and by the German-Czech exchange project grant of the Deutsche Akademischer Auslandsdienst (DAAD-19-03) to M.H. and M.F. The cooperation with JINR Dubna was supported by the grants from the MEYS CR to MF (The Projects of the Czech Plenipotentiary and the 3-Plus-3 Project).

ACKNOWLEDGMENTS

The authors thank Harry Scherthan, Bundeswehr Institute for Radiobiology, Munich, for his help in urgent cases of material delivery and for many fruitful discussions.

REFERENCES

1. Chancellor J, Scott G, Sutton J. Space Radiation: the number one risk to astronaut health beyond low earth orbit. *Life* (2014) **4**:491–510. doi:10.3390/life4030491
2. Kennedy AR. Biological effects of space radiation and development of effective countermeasures. *Life Sci Space Res* (2014) **1**:10–43. doi:10.1016/j.lssr.2014.02.004
3. Walsh L, Schneider U, Fogtman A, Kausch C, McKenna-Lawlor S, Narici L, et al. Research plans in Europe for radiation health hazard assessment in exploratory space missions. *Life Sci Space Res* (2019) **21**:73–82. doi:10.1016/j.lssr.2019.04.002
4. Durante M, Orecchia R, Loeffler JS. Charged-particle therapy in cancer: clinical uses and future perspectives. *Nat Rev Clin Oncol* (2017) **14**:483–95. doi:10.1038/nrclinonc.2017.30
5. Rackwitz T, Debus J. Clinical applications of proton and carbon ion therapy. *Semin Oncol* (2019) **46**:226–32. doi:10.1053/j.seminoncol.2019.07.005
6. Falk M, Lukasova E, Gabrielova B, Ondrej V, Kozubek S. Chromatin dynamics during DSB repair. *Biochim Biophys Acta* (2007) **1773**:1534–45. doi:10.1016/j.bbamcr.2007.07.002
7. Falk M, Lukášová E, Kozubek S. Chromatin structure influences the sensitivity of DNA to γ-radiation. *Biochim Biophys Acta* (2008) **1783**:2398–414. doi:10.1016/j.bbamcr.2008.07.010

8. Falk M, Lukasova E, Kozubek S. Higher-order chromatin structure in DSB induction, repair and misrepair. *Mutat Res* (2010 Apr-Jun) **704** (1-3):88–100. doi:10.1016/j.mrrev.2010.01.013.
9. Falk M, Hausmann M, Lukášová E, Biswas A, Hildenbrand G, Davídková M, et al. Determining omics spatiotemporal dimensions using exciting new nanoscopy techniques to assess complex cell responses to DNA damage: part A-radiomics. *Crit Rev Eukaryot Gene Expr* (2014) **24**:205–23. doi:10.1615/critreveukaryotgeneexpr.2014010313
10. Falk M, Hausmann M, Lukášová E, Biswas A, Hildenbrand G, Davídková M, et al. Determining omics spatiotemporal dimensions using exciting new nanoscopy techniques to assess complex cell responses to DNA damage: part B-structuromics. *Crit Rev Eukaryot Gene Expr* (2014) **24**:225–47. doi:10.1615/critreveukaryotgeneexpr.v24.i3.40
11. Chancellor JC, Auñon-Chancellor SM, Charles J. Medical Implications of Space Radiation Exposure Due to Low-Altitude Polar Orbits. *Aerosp Med Hum Perf* (2018) **89**:3–8. doi:10.3357/amhp.4956.2018
12. Bilski P, Marczewska B, Gieszczyk W, Kłosowski M, Naruszewicz M, Sankowska M, Kodaira S. Fluorescent imaging of heavy charged particle tracks with LiF single crystals. *J Lumin* (2019) **213**:82–7. doi:10.1016/j.jlumin.2019.05.007
13. Jacob B, Taucher-Scholz G. Interaction of heavy ions with nuclear chromatin: spatiotemporal investigations of biological responses in a cellular environment. *Nucl Instrum Methods Phys Res B* (2006) **245**:292–7. doi:10.1016/j.nimb.2005.11.117
14. Jezkova L, Zadneprianetc M, Kulikova E, Smirnova E, Bulanova T, Depes D, et al. Particles with similar LET values generate DNA breaks of different complexity and reparability: a high-resolution microscopy analysis of γH2AX/53BP1 foci. *Nanoscale* (2018) **10**:1162–79. doi:10.1039/c7nr06829h
15. Depes D, Lee J-H, Bobkova E, Jezkova L, Falkova I, Bestvater F, et al. Single molecule localization microscopy as a promising tool for γH2AX/53BP1 foci exploration. *Eur Phys J D* (2018) **72**:158. doi:10.1140/epjd/e2018-90148-1
16. Nikitaki Z, Nikolov V, Mavragani IV, Mladenov E, Mangelis A, et al. Measurement of complex DNA damage induction and repair in human cellular systems after exposure to ionizing radiations of varying linear energy transfer (LET). *Free Radic Res* (2016) **50**:64–78. doi:10.1080/10715762.2016.1232484
17. Schipler A, Iliakis G. DNA double-strand-break complexity levels and their possible contributions to the probability for error-prone processing and repair pathway choice. *Nucleic Acids Res* (2013) **41**:7589–605. doi:10.1093/nar/gkt556
18. Mladenov E, Magin S, Soni A, Iliakis G. DNA double-strand-break repair in higher eukaryotes and its role in genomic instability and cancer: cell cycle and proliferation-dependent regulation. *Semin Canc Biol* (2016) **37–38**:51–64. doi:10.1016/j.semcancer.2016.03.003
19. Ceccaldi R, Rondinelli B, D'Andrea AD. Repair pathway choices and consequences at the double-strand break. *Trends Cell Biol* (2016) **26**:52–64. doi:10.1016/j.tcb.2015.07.009
20. Dueva R, Iliakis G. Alternative pathways of non-homologous end joining (NHEJ) in genomic instability and cancer. *Transl Cancer Res* (2013) **2**:163–77. doi:10.3978/j.issn.2218-676X.2013.05.02
21. Mladenov E, Magin S, Soni A, Iliakis G. DNA double-strand break repair as determinant of cellular radiosensitivity to killing and target in radiation therapy. *Front Oncol* (2013) **3**:113. doi:10.3389/fonc.2013.00113
22. Bhattacharjee S, Nandi S. Synthetic lethality in DNA repair network: a novel avenue in targeted cancer therapy and combination therapeutics. *IUBMB Life* (2017) **69**:929–37. doi:10.1002/iub.1696
23. Jeggo PA, Löbrich M. How cancer cells hijack DNA double-strand break repair pathways to gain genomic instability. *Biochem J* (2015) **471**:1–11. doi:10.1042/bj20150582
24. Rogakou EP, Pilch DR, Orr AH, Ivanova VS, Bonner WM. DNA Double-stranded Breaks Induce Histone H2AX Phosphorylation on Serine 139. *J Biol Chem* (1998) **273**:5858–68. doi:10.1074/jbc.273.10.5858
25. Kinner A, Wu W, Staudt C, Iliakis G. Gamma-H2AX in recognition and signaling of DNA double-strand breaks in the context of chromatin. *Nucleic Acids Res* (2008) **36**:5678–94. doi:10.1093/nar/gkn550
26. Chang HHY, Pannunzio NR, Adachi N, Lieber MR. Non-homologous DNA end joining and alternative pathways to double-strand break repair. *Nat Rev Mol Cell Biol* (2017) **18**:495–506. doi:10.1038/nrm.2017.48
27. Iliakis G, Murmann T, Soni A. Alternative end-joining repair pathways are the ultimate backup for abrogated classical non-homologous end-joining and homologous recombination repair: implications for the formation of chromosome translocations. *Mutat Res Genet Toxicol Environ Mutagen* (2015) **793**:166–75. doi:10.1016/j.mrgentox.2015.07.001
28. Jasin M, Rothstein R. Repair of strand breaks by homologous recombination. *Cold Spring Harb Perspect Biol* (2013) **5**:a012740. doi:10.1101/cshperspect.a012740
29. Shibata A, Jeggo PA. Canonical DNA non-homologous end-joining; capacity versus fidelity. *Br J Radiol* (2020) **23**:20190966. doi:10.1259/bjr.20190966
30. Löbrich M, Jeggo P. A process of resection-dependent nonhomologous end joining involving the Goddess Artemis. *Trends Biochem Sci* (2017) **42**:690–701. doi:10.1016/j.tibs.2017.06.011
31. Rothkamm K, Krüger I, Thompson LH, Löbrich M. Pathways of DNA double-strand break repair during the mammalian cell cycle. *Mol Cell Biol* (2003) **23**:5706–15. doi:10.1128/mcb.23.16.5706-5715.2003
32. Shrivastav M, De Haro LP, Nickoloff JA. Regulation of DNA double-strand break repair pathway choice. *Cell Res* (2008) **18**: 134–47. doi:10.1038/cr.2007.111
33. Goodarzi AA, Noon AT, Jeggo PA. The impact of heterochromatin on DSB repair. *Biochem Soc Trans* (2009) **37**:569–76. doi:10.1042/bst0370569
34. Goodarzi AA, Jeggo P, Lobrich M. The influence of heterochromatin on DNA double strand break repair: getting the strong, silent type to relax. *DNA Repair* (2010) **9**:1273–82. doi:10.1016/j.dnarep.2010.09.013
35. Brandsma I, Gent DC. Pathway choice in DNA double strand break repair: observations of a balancing act. *Genome Integr* (2012) **3**:9. doi:10.1186/2041-9414-3-9
36. Aparicio T, Baer R, Gautier J. DNA double-strand break repair pathway choice and cancer. *DNA Repair* (2014) **19**:169–75. doi:10.1016/j.dnarep.2014.03.014
37. Kakarougkas A, Jeggo PA. DNA DSB repair pathway choice: an orchestrated handover mechanism. *Br J Radiol* (2014) **87**:20130685. doi:10.1259/bjr.20130685
38. Clouaire T, Legube G. DNA double strand break repair pathway choice: a chromatin based decision? *Nucleus* (2015) **6**:107–13. doi:10.1080/19491034.2015.1010946
39. Maier P, Hartmann L, Wenz F, Herskind C. Cellular pathways in response to ionizing radiation and their targetability for tumor radiosensitization. *Int J Mol Sci* (2016) **17**:102. doi:10.3390/ijms17010102
40. Li J, Xu X. DNA double-strand break repair: a tale of pathway choices. *Acta Biochim Biophys Sin* (2016) **48**:641–6. doi:10.1093/abbs/gmw045
41. Majidinia M, Yousefi B. DNA repair and damage pathways in breast cancer development and therapy. *DNA Repair* (2017) **54**:22–9. doi:10.1016/j.dnarep.2017.03.009
42. Janssen A, Colmenares SU, Lee T, Karpen GH. Timely double-strand break repair and pathway choice in pericentromeric heterochromatin depend on the histone demethylase dKDM4A. *Genes Dev* (2019) **33**:103–15. doi:10.1101/gad.317537.118
43. Cremer T, Cremer M, Hübner B, Strickfaden H, Smeets D, Popken J, et al. The 4D nucleome: evidence for a dynamic nuclear landscape based on co-aligned active and inactive nuclear compartments. *FEBS Lett* (2015) **589**:2931–43. doi:10.1016/j.febslet.2015.05.037
44. Cremer T, Cremer M, Hübner B, Silahtaroglu A, Hendzel M, Lanctôt CH, et al. The interchromatin compartment participates in the structural and functional organization of the cell nucleus. *BioEssays* (2020) **42**:1900132. doi:10.1002/bies.201900132
45. Strickfaden Y, Máté G, Müller P, Hillebrandt S, Krufczik M, Bach MR, et al. Radiation induced chromatin conformation changes analysed by fluorescent localization microscopy, statistical physics, and graph theory. *PLoS One* (2015) **10**:e0128555. doi:10.1371/journal.pone.0128555
46. Kaufmann K, Barnard S, Moquet J, Ellender M, Rana Z, Burdak-Rothkamm S. DNA damage foci: meaning and significance. *Environ Mol Mutagen* (2015) **56**:491–504. doi:10.1002/em.21944
47. Schumann S, Eberlein U, Muller J, Scherthan H, Lassmann M. Correlation of the absorbed dose to the blood and DNA damage in leukocytes after internal *ex-vivo* irradiation of blood samples with Ra-224. *Eur J Nucl Med Mol I* (2018) **8**:77. doi:10.1186/s13550-018-0422-4.
48. Rübe CE, Lorat Y, Schuler N, Schanz S, Wennemuth G, Rübe C. DNA repair in the context of chromatin: new molecular insights by the nanoscale detection of

DNA repair complexes using transmission electron microscopy. *DNA Repair* (2011) **10**:427–37. doi:10.1016/j.dnarep.2011.01.012
49. Lorat Y, Brunner CU, Schanz S, Jakob B, Taucher-Scholz G, Rübe CE. Nanoscale analysis of clustered DNA damage after high-LET irradiation by quantitative electron microscopy-the heavy burden to repair. *DNA Repair* (2015) **28**:93–106. doi:10.1016/j.dnarep.2015.01.007
50. Timm S, Lorat Y, Jakob B, Taucher-Scholz G, Rübe CE. Clustered DNA damage concentrated in particle trajectories causes persistent large-scale rearrangements in chromatin architecture. *Radiother Oncol* (2018) **129**: 600–10. doi:10.1016/j.radonc.2018.07.003
51. Cremer C, Masters BR. Resolution enhancement techniques in microscopy. *Eur Phys J H* (2013) **38**:281–344. doi:10.1140/epjh/e2012-20060-1
52. Cremer C, Birk U. Perspectives in super-resolved fluorescence microscopy: what comes next? *Front Phys* (2016) **4**:11. doi:10.3389/fphy.2016.00011
53. Hausmann M, Ilić N, Pilarczyk G, Lee J-H, Logeswaran A, Borroni AM, et al. Challenges for super-resolution localization microscopy and biomolecular fluorescent nano-probing in cancer research. *Int J Mol Sci* (2017) **18**:2066. doi:10.3390/ijms18102066
54. Krufczik M, Wagner E, Lee J-H, Schrock G, Schaufler W, Krufczik M, et al. Super-resolution localization microscopy of radiation-induced histone H2AX-phosphorylation in relation to H3K9-trimethylation in HeLa cells. *Nanoscale* (2018) **10**:4320–31. doi:10.1039/c7nr08145f
55. Bobkova E, Depes D, Lee J-H, Jezkova L, Falkova I, Pagacova E, et al. Recruitment of 53BP1 proteins for DNA repair and persistence of repair clusters differ for cell types as detected by single molecule localization microscopy. *Int J Mol Sci* (2018) **19**:3713. doi:10.3390/ijms19123713
56. Scherthan H, Lee J-H, Maus E, Schumann S, Muhtadi R, Chojowski R, et al. Nanostructure of clustered DNA damage in leukocytes after in-solution irradiation with the alpha emitter Ra-223. *Cancers* (2019) **11**:1877. doi:10.3390/cancers11121877
57. Costes SV, Boissière A, Ravani S, Romano R, Parvin B, Barcellos-Hoff MH. Imaging features that discriminate between foci induced by high- and low-LET radiation in human fibroblasts. *Radiat Res* (2006) **165**:505–15. doi:10.1667/rr3538.1
58. Hauptner A, Friedland W, Dietzel S, Drexler GA, Greubel C, Hable V, et al. Spatial distribution of DNA double-strand breaks from ion tracks. *Ion beam science: solved and unsolved problems*. Copenhagen, Denmark: Royal Danish Academy of Sciences and Letters (2006) p. 59–85.
59. Hable V, Drexler GA, Brüning T, Burgdorf C, Greubel C, Derer A, et al. Recruitment kinetics of DNA repair proteins Mdc1 and Rad52 but not 53BP1 depend on damage complexity. *PLoS One* (2012) **7**:e41943. doi:10.1371/journal.pone.0041943
60. Lorat Y, Timm S, Jacob B, Taucher-Scholz G, Rübe CE. Clustered double-strand breaks in heterochromatin perturb DNA repair after high linear energy transfer irradiation. *Radiother Oncol* (2016) **121**:427–37. doi:10.1016/j.radonc.2016.08.028
61. Perez RL, Best G, Nicolay NH, Greubel C, Rossberger S, Reindl J, et al. Superresolution light microscopy shows nanostructure of carbon ion radiation-induced DNA double-strand break repair foci. *FASEB J* (2016) **30**:2767–76. doi:10.1096/fj.201500106r
62. Natale F, Rapp A, Yu W, Maiser A, Harz H, Schall A, et al. Identification of the elementary structural units of the DNA damage response. *Nat Commun* (2018) **8**:15760. doi:10.1038/ncomms15760
63. Reindl JS, Girst S, Walsh DWM, Geubel C, Schwarz B, Siebenwirth C, et al. Chromatin organization revealed by nanostructure of irradiation inducedγH2AX, 53BP1 and Rad51 foci. *Sci Rep* (2017) **7**:40616. doi:10.1038/srep40616.
64. Eryilmaz M, Schmitt E, Krufczik M, Theda F, Lee J-H, Cremer CF, et al. Localization microscopy analyses of MRE11 clusters in 3D-conserved cell nuclei of different cell lines. *Cancers* (2018) **10**:25. doi:10.3390/cancers10010025
65. Bestvater D, Memmel S, Doose S, Neubauer J, Zimmermann H, Flentje M, et al. Nanostructure of DNA repair foci revealed by superresolution microscopy. *FASEB J* (2018) **12**:fj201701435. doi:10.1096%2Ffj.201701435
66. Hofmann A, Krufczik M, Heermann D, Hausmann M. Using persistent homology as a new approach for super-resolution localization microscopy data analysis and classification of γH2AX foci/clusters. *Int J Mol Sci* (2018) **19**: 2263. doi:10.3390/ijms19082263
67. Kakarougkas A, Ismail A, Klement K, Goodarzi AA, Conrad S, Freire R, et al. Opposing roles for 53BP1 during homologous recombination. *Nucleic Acids Res* (2013) **41**:9719–31. doi:10.1093/nar/gkt729
68. Chapman JR, Taylor MRG, Boulton SJ. Playing the end game: DNA double-strand break repair pathway choice. *Mol Cell* (2012) **47**:497–510. doi:10.1016/j.molcel.2012.07.029
69. Reindl J, Drexler GA, Girst S, Greubel C, Siebenwirth C, Drexler SE, et al. Nanoscopic exclusion between Rad51 and 53BP1 after ion irradiation in human HeLa cells. *Phys Biol* (2015) **12**:066005. doi:10.1088/1478-3975/12/6/066005
70. Lemmer P, Gunkel M, Baddeley D, Kaufmann R, Urich A, Weiland YJ, et al. SPDM: light microscopy with single-molecule resolution at the nanoscale. *Appl Phys B* (2008) **93**:1–12. doi:10.1007/s00340-008-3152-x
71. Reymann P, Gunkel M, Weiland Y, Müller P, Baddeley D, Kaufmann RA, et al. Using conventional fluorescent markers for far-field fluorescence localization nanoscopy allows resolution in the 10-nm range. *J Microsc* (2009) **235**:163–71. doi:10.1111/j.1365-2818.2009.03196.x
72. Eberle JP, Rapp A, Krufczik M, Eryilmaz M, Gunkel M, et al. Super-resolution microscopy techniques and their potential for applications in radiation biophysics. In: H Erfle, editor *Super-resolution microscopy–methods and protocols. Methods in Molecular Biology*. **Vol. 1663**. New York, NY: Humana Press (2017) p. 1–13.
73. Bach M, Savini C, Krufczik M, Cremer C, Rösl F, Hausmann M. Super-resolution localization microscopy of γ-H2AX and heterochromatin after folate deficiency. *Int J Mol Sci* (2017) **18**:1726. doi:10.3390/ijms18081726
74. Aguilar M, Cavasonza A, Alpat B, Ambrosi G, Arruda L, Attig N, et al. AMS Collaboration. Precision measurement of cosmic-ray nitrogen and its primary and secondary components with the alpha magnetic spectrometer on the International Space Station. *Phys Rev Lett* (2018) **121**:051103. doi:10.1103%2FPhysRevLett.121.051103
75. Mathew KJ, Murty SVS. Cosmic ray produced nitrogen in extra terrestrial matter. *J Earth Syst Sci* (1993) **102**:415–37. doi:10.1007%2FBF02841731
76. McDonald FB, Teegarden BJ, Trainor JH, Webber WR. The anomalous abundance of cosmic-ray nitrogen and oxygen nuclei at low energies. *Astrophys J* (1974) **187**:L105. doi:10.1086/181407
77. Ying C, Bolst D, Rosenfeld A, Guatelli S. Characterization of the mixed radiation field produced by carbon and oxygen ion beams of therapeutic energy: a Monte Carlo simulation study. *J Med Phys* (2019) **44**:263–9. doi:10.4103/jmp.jmp_40_19
78. Tran LT, Bolst D, Guatelli S, Pogossov A, Petasecca M, Lerch MLF, et al. The relative biological effectiveness for carbon, nitrogen, and oxygen ion beams using passive and scanning techniques evaluated with fully 3D silicon microdosimeters. *Med Phys* (2018) **45**:2299–308. doi:10.1002/mp.12874
79. Bezbakh AA, Zager VB, Kaminski G, Krylov AI, Krylov VA, Teterev YG, et al. Upgrading the genome facility for radiobiological experiments with heavy-ion beams. *Phys Part Nucl Lett* (2013) **10**:175–8. doi:10.1134%2FS1547477113020039
80. Jakob B, Scholz M, Taucher-Scholz G. Biological imaging of heavy charged-particle tracks. *Radiat Res* (2003) **159**:676–84. doi:10.1667/0033-7587(2003)159[0676:biohct]2.0.co;2
81. Tarasov OB, Bazin D. LISE++: exotic beam production with fragment separators and their design. *Nucl Instrum Methods Phys Res B* (2016) **376**: 185–7. doi:10.1016%2Fj.nimb.2016.03.021
82. Krufczik M, Sievers A, Hausmann A, Lee J-H, Hildenbrand G, Schaufler W, et al. Combining low temperature fluorescence DNA-hybridization, immunostaining, and super-resolution localization microscopy for nano-structure analysis of ALU elements and their influence on chromatin structure. *Int J Mol Sci* (2017) **18**: 1005. doi:10.3390/ijms18051005
83. Stuhlmüller M, Schwarz-Finsterle J, Fey E, Lux J, Bach M, Cremer CK, et al. *In situ* optical sequencing and structure analysis of a trinucleotide repeat genome region by localization microscopy after specific COMBO-FISH nano-probing. *Nanoscale* (2015) **7**:17938–46. doi:10.1039/c5nr04141d
84. Hinderhofer BD. Modelling Spatial Patterns. *J R Stat Soc B* (1977) **39**:172–92. doi:10.1111/j.2517-6161.1977.tb01615.x
85. Ester M, Kriegel HP, Sander G, Xu X. A density-based algorithm for discovering clusters a density-based algorithm for discovering clusters in large spatial databases with noise. In: Proceedings of the second international conference on knowledge discovery and data mining; 4–8 August 1996; Portland, OR; p. 226–31. Available from: https://www.aaai.org/Papers/KDD/1996/KDD96-037.pdf

86. Máté G, Hofmann A, Wenzel N, Heermann DW. A topological similarity measure for proteins. *Biochim Biophys Acta* (2014) **1838**:1180–90. doi:10.1016/j.bbamem.2013.08.019
87. Ghrist R. Barcodes: the persistent topology of data. *Bull Am Math Soc* (2007) **45** (01):61–76. doi:10.1090/s0273-0979-07-01191-3
88. Jaccard P. Etude comparative de la distribution florale dans une portion des Alpes et des Jura. *Bull Soc Vaud Sci Nat* (1901) **37**:547–79. doi:10.5169%2Fseals-266450
89. Schwarz B, Friedl AA, Girst S, Dollinger G, Reindl J. Nanoscopic analysis of 53BP1, BRCA1 and Rad51 reveals new insights in temporal progression of DNA-repair and pathway choice. *Mutat Res* (2019) **816**–**818**:111675. doi:10.1016/j.mrfmmm.2019.111675
90. Kumar R, Horikoshi N, Singh M, Gupta A, Misra HS, Albuquerque K, et al. Chromatin modifications and the DNA damage response to ionizing radiation. *Front Oncol* (2012) **2**:214. doi:10.3389/fonc.2012.00214
91. Hunt JR, Sossick AJ, Boulton SJ, Jackson SP. BRCA1-associated exclusion of 53BP1 from DNA damage sites underlies temporal control of DNA repair. *J Cell Sci* (2012) **125**:3529–34. doi:10.1242/jcs.105353

Conflict of Interest: The authors declare that the research was conducted in the absence of any commercial or financial relationships that could be construed as a potential conflict of interest.